

Anuradha Godavarty, PhD  
Margaret J. Eppstein, PhD  
Chaoyang Zhang, PhD  
Eva M. Sevick-Muraca, PhD

Published online  
10.1148/radiol.2343031725  
Radiology 2005; 235:148–154

**Abbreviations:**

AEKF = approximate extended  
Kalman filter  
CCD = charge-coupled device  
ICG = indocyanine green  
NIR = near-infrared  
T:B = target to background  
3D = three-dimensional

<sup>1</sup> From the Photon Migration Laboratories, Texas A&M University, PO Box 30012, College Station, TX 77842-3012 (A.G., E.M.S.M.); and Department of Computer Science, University of Vermont, Burlington, Vermont (M.J.E., C.Z.). Received October 29, 2003; revision requested January 12, 2004; revision received April 30; accepted May 24. Supported in part by NIH R01 CA67176 and NIH R01 EB002763. **Address correspondence to** E.M.S.M. (e-mail: [eva-m-sevick@tamu.edu](mailto:eva-m-sevick@tamu.edu)).

Authors stated no financial relationship to disclose.

**Author contributions:**

Guarantors of integrity of entire study, all authors; study concepts, A.G., E.M.S.M.; study design, all authors; literature research, A.G., E.M.S.M.; experimental studies, A.G., E.M.S.M.; data acquisition, A.G., E.M.S.M.; data analysis/interpretation, all authors; manuscript preparation, definition of intellectual content, editing, revision/review, and final version approval, all authors

© RSNA, 2005

# Detection of Single and Multiple Targets in Tissue Phantoms with Fluorescence-enhanced Optical Imaging: Feasibility Study<sup>1</sup>

**PURPOSE:** To evaluate the feasibility of reconstructing single and multiple targets by using fluorescence-enhanced tomography of a breast tissue phantom.

**MATERIALS AND METHODS:** Frequency-domain fluorescence measurements were performed in cup-shaped tissue phantoms of clinically relevant size (diameter, 10 cm) in which single or multiple 0.5–1.0-cm<sup>3</sup> targets that contained micromolar concentrations of indocyanine green with 1:0 and 100:1 target-to-background (T:B) contrast ratios had been embedded. Rapid acquisition of time-dependent fluorescent light measurements was performed at the phantom surface in response to point illumination of excitation light by using a gain-modulated intensified charge-coupled device detection system. Boundary surface measurements were used to tomographically reconstruct the interior targets located with various experimental conditions.

**RESULTS:** Single 1.0-cm<sup>3</sup> targets located between 1.43 and 2.82 cm deep from the phantom surface at a T:B contrast ratio of 100:1 and three approximately 0.55-cm<sup>3</sup> targets located about 1.30 cm deep at a T:B contrast ratio of 1:0 were reconstructed with minimal or no artifacts by using boundary surface fluorescence measurements and an approximate extended Kalman filter algorithm.

**CONCLUSION:** It is feasible to detect single or multiple fluorescent targets in tissue phantoms of clinically relevant size by using fluorescence-enhanced optical tomography.

© RSNA, 2005

Supplemental material: [radiology.rsna.org/cgi/content/full/234/3/148/DC1](http://radiology.rsna.org/cgi/content/full/234/3/148/DC1)

Imaging plays a central role in cancer diagnosis, therapy, and prognosis primarily through the depiction of anatomically defined abnormalities. With the wealth of information provided by the maturing fields of genomics and proteomics, the identification of molecular markers and targets promises contrast material-enhanced diagnostic imaging with specificity and sensitivity that is not otherwise possible with conventional anatomic imaging (1). If measurement approaches can result in the acquisition of signals from micromolar or smaller amounts of contrast agents within clinically relevant volumes, molecular imaging promises to improve diagnostic imaging and to affect the quality of care for patients with cancer.

Near-infrared (NIR) light between the wavelengths of 700 and 900 nm propagates deeply through tissues and provides a unique approach for molecularly based diagnostic imaging. With NIR-excitable fluorescent contrast agents that can be conveniently conjugated with a targeting or reporting moiety, there is clinical opportunity (yet unproved) for using nonionizing radiation with these nonradioactive contrast agents for “homing in on” early

metastatic lesions, performing sentinel lymph node mapping, and following the progress of therapy. Furthermore, if one conducts measurements with emerging time-dependent techniques in which fluorescent decay processes are measured, the ability to employ activate-able fluorescent contrast agents and to tomographically reconstruct three-dimensional (3D) in vivo maps of diseased tissue may be possible. To date, limited progress toward 3D tomographic fluorescence-enhanced optical imaging has been demonstrated in phantom-based and small animal-based studies (2–6).

The translation of fluorescence-enhanced optical imaging to the clinic is made possible by the availability of indocyanine green (ICG), with its established record of nontoxicity and patient safety for the indications of evaluating hepatic function (7) and retinal angiography (8), as a potential NIR fluorescent contrast agent. However, before ICG can be used in fluorescence-enhanced optical imaging, tissue phantom studies must be performed to demonstrate the possible benefits. The purpose of our study was to demonstrate the feasibility of reconstructing single and multiple targets by using fluorescence-enhanced tomography of a breast-shaped phantom.

## MATERIALS AND METHODS

### Phantoms

A cup-shaped phantom (10-cm-diameter hemisphere, 262-cm<sup>3</sup> volume) filled with a fatty emulsion liquid (1% Liposyn; Abbott Laboratories, North Chicago, Ill) was used to mimic the breast tissue (Fig 1). The extended 20-cm-diameter cylindrical portion of the breast phantom (825-cm<sup>3</sup> volume) represented the chest wall regions around the breast tissue.

Measurements for image reconstruction were performed by using single or multiple 0.5–1.0-cm<sup>3</sup> targets (transparent cubical cuvettes or hand-blown glass spheres filled with appropriate concentrations of the fluorescing contrast agent in 1% Liposyn solution) that were located at different depths and target-to-background (T:B) contrast ratios, as listed in Table 1. In the first three experiments, 1  $\mu\text{mol/L}$  of ICG (Cardio-Green; Akorn, Buffalo Grove, Ill) in 1% Liposyn solution was used in the target, and 0.01  $\mu\text{mol/L}$  of ICG was used in the background, which contained 1% Liposyn, to mimic tissue scattering properties. In other words, in the first three experiments, an imperfect uptake (T:B contrast

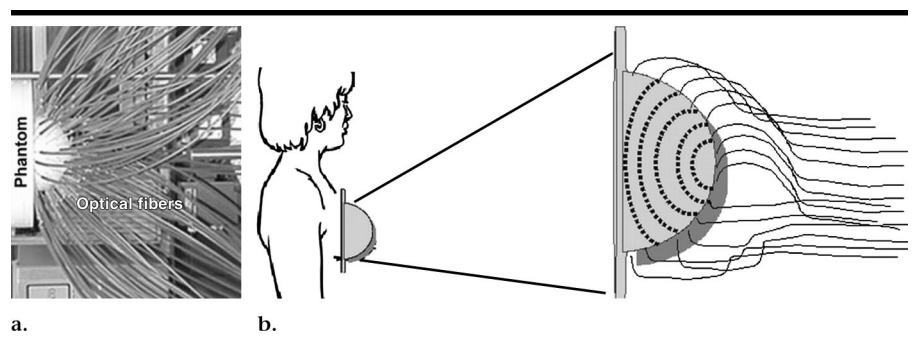


**Figure 1.** (a) Cup-shaped breast phantom. The cylindrical portion represents the extended chest wall regions. Optical fibers of 1 mm in diameter were placed in concentric rings along the hemispheric surface of the breast phantom to illuminate and collect light signals. (b) Schematic of possible device for clinical breast imaging.

ratio, 100:1) of the fluorescing contrast agent by the target was assumed. For the fourth experiment, three approximately 0.55-cm<sup>3</sup> targets containing 2.5  $\mu\text{mol/L}$  of ICG were positioned within the phantom, which contained no ICG; hence, with this situation, a perfect uptake (T:B contrast ratio, 1:0) of the contrast agent was assumed. ICG excites at 780 nm and emits at 830 nm; it has a fluorescent lifetime of 0.56 nsec and a quantum efficiency of 0.016 (9).

### Frequency-Domain Photon Migration Measurements

Time-dependent measurements of fluorescent light propagation and generation were made by using frequency-domain techniques. Briefly, this method depends on illuminating the phantom with intensity-modulated excitation light and detecting the phase delay and amplitude attenuation of the generated fluorescent light relative to the phase delay and amplitude of the incident excitation light. The phase delay is effectively a measurement of the mean total time of light propagation and fluorescence generation. The phantom surfaces were sequentially illuminated at single point positions on the phantom surface with intensity-modulated excitation light (783 nm at a 100-MHz modulation frequency) by using 1000- $\mu\text{m}$ -diameter optical fibers to deliver the light. The fluorescent signal (830 nm) was collected from point locations on the phantom surface through the 1000- $\mu\text{m}$ -diameter optical fibers and by using interference (830 nm) and holographic (780 nm) filters to block the excitation light.

Rapid acquisition of the phase delay and amplitude modulation of the detected fluorescent light emitted from the end of each collecting fiber was simultaneously accomplished by using a gain-

modulated intensified charge-coupled device (CCD) camera, which was operated in homodyne detection mode. A schematic of the frequency-domain photon migration-modulated intensified CCD camera system is provided in Figure 2, and details pertaining to instrumentation and the data acquisition procedure are described in Appendix E1 at [radiology.rsna.org/cgi/content/full/234/3/148/DC1](http://radiology.rsna.org/cgi/content/full/234/3/148/DC1) and elsewhere (6,10–12). With the intensified CCD system, fluorescent boundary surface measurements of phase delay and amplitude attenuation were acquired from sparse point locations on the hemispheric surface and used along with a finite-element-based (13) diffusion model for light propagation in tissues (14–16) so that we could reconstruct the position of the target(s).

### Reconstruction Algorithms

Three-dimensional image reconstructions of the tissue phantom were created from sparse surface measurements of the fluorescence signal emitted from the small targets that contained ICG. The unknown vector of absorption coefficient,  $\mu_{\text{axf}}$ , due to the presence of the fluorescing agent was reconstructed by using a recursively updating Bayesian algorithm, yielding an interior optical property map. Table 1 lists the number of paired phase-shift and amplitude attenuation measurements, as well as the number of unknowns, or vector elements of  $\mu_{\text{axf}}$ .

Unlike the simple back-projection schemes used in conventional computed tomographic (CT) or nuclear imaging techniques, optical image reconstructions are based on the diffusive transport of light in a highly scattering medium and require nonlinear reconstruction techniques. The reconstruction algorithm used in this study, the approximate extended Kalman filter

**TABLE 1**  
Experimental Parameters for Various Measurements in the Four Imaging Experiments

Experiment No.	Target Volume (cm <sup>3</sup> )	Target Shape	T:B Ratio	Target Depth (cm)	No. of Targets	No. of Measurements*	No. of Unknowns During Reconstructions†
1	1.0	Cube	100:1	1.43	1	401	3857
2	1.0	Cube	100:1	2.04	1	480	3857
3	1.0	Cube	100:1	2.82	1	480	3857
4	About 0.55	Sphere	1:0	About 1.30	3	286	3857, 11 906

\* As phase-amplitude pairs.

† The number of unknowns represents the number of vector elements of  $\mu_{axf}$ .

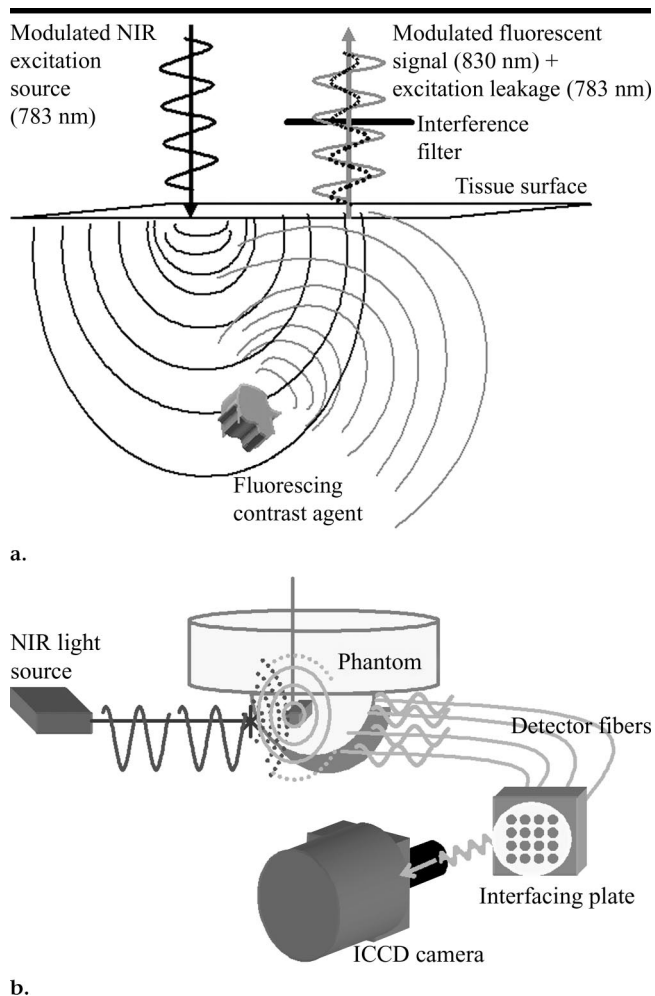


**Figure 2.** (a) Frequency-domain photon migration measurement technique, which entails the use of point illumination and point detection measurement geometry. (b) Schematic of the operation of the intensified CCD (ICCD) imaging system when phantom volumes are used.

(AEKF), involves the use of a Bayesian approach, in which the statistics of measurement errors, along with the acquired fluorescence measurements, are used to optimally reconstruct the 3D fluorescence absorption coefficient distribution in the entire breast phantom. Details of the reconstruction algorithm are pro-

vided in Appendix E2 at [radiology.rsna.org/cgi/content/full/234/3/148/DC1](http://radiology.rsna.org/cgi/content/full/234/3/148/DC1) and elsewhere (3,6,17).

### Data Analysis

The sparse boundary surface fluorescence measurements, along with the

measurement errors in the AEKF reconstruction algorithm, were used to reconstruct the absorption coefficient,  $\mu_{axf}$ , due to the fluorophore in the hemispheric portion of the 3D phantom volume. A constant value of  $\mu_{axf}$ ,  $0.003 \text{ cm}^{-1}$ , was chosen as the initial estimate of the reconstruction parameter for all the experimental cases during the image reconstructions, and the AEKF algorithm was performed iteratively with a 3.06-GHz Pentium IV machine (Xeon; Dell Computers, Dallas, Tex) to estimate the spatial distribution of  $\mu_{axf}$  in the phantom volume. Convergence on the final absorption image occurred when there was less than a 1% additional decrease in the root-mean-square output error.

In all of the experiments, the target was differentiated from the background tissue phantom on the basis of the first break (termed the "threshold" value) observed in the histogram distribution of the reconstructed parameter  $\mu_{axf}$ . The spatial distribution of the reconstructed parameter  $\mu_{axf}$  above the threshold value was plotted as a series of points located in 3D space in the anterior and lateral views of the 3D breast phantom by using Tecplot 9.2 software (Amtech Engineering, Bellevue, Wash).

On the basis of the threshold values in the reconstructed parameter  $\mu_{axf}$ , the centroid of the reconstructed target(s) and the difference between the actual and the reconstructed target positions, along with the reconstructed volume, were estimated. The difference between the actual and the reconstructed target positions was estimated as the Euclidean distance between the value-weighted centroids of the reconstructed and actual target locations. The reconstructed volume was calculated as the sum of the volumes corresponding to the nodes of the finite-element mesh that had a  $\mu_{axf}$  that was greater than the set threshold value.

In the case of the fourth experiment, which involved small-volume targets of approximately  $0.55 \text{ cm}^3$ , two finite-ele-

**TABLE 2**  
**Details of Image Reconstruction Times and Iterations for All Experiments**

Experiment No.	Finite-Element Mesh		No. of Unknowns*	No. of Knowns†	Reconstruction Time per Iteration (min)	No. of Iterations for Convergence
	No. of Nodes	No. of Elements				
1	6956	33 413	3857	401	5.6	5
2	6956	33 413	3857	480	6.9	5
3	6956	33 413	3857	480	5.7	13
4	6956	33 413	3857	286	2.9	14
4	18 105	94 767	11 906	286	14.9	27

\* Corresponds to number of nodal points in finite-element mesh where the reconstructed parameter was evaluated.

† Corresponds to total number of source-detector measurement pairs acquired during experiment.

ment meshes, varying in their level of discretization (3857 and 11 906 unknowns), were used to determine the effect of discretization on image reconstruction of small-volume targets.

## RESULTS

The absorption coefficient,  $\mu_{axf}$ , due to the fluorophore was successfully reconstructed for all of the experiments by using the AEKF reconstruction algorithm. The total reconstruction time was a function of the total number of measurements and the finite-element mesh discretization and varied nonlinearly with respect to these numbers of knowns and unknowns, respectively. On average, each iteration required 5–7 minutes when the number of unknowns was 3857. However, when a finely discretized mesh with 11 906 unknowns was used in the fourth experiment, each iteration required approximately 15 minutes. The reconstruction times and numbers of iterations required for convergence are tabulated in Table 2.

Anterior and lateral views of the tissue phantom containing the true and reconstructed targets in the four experimental cases are shown in Figures 3–6 as the spatial distribution of nodal points in which the reconstructed parameter  $\mu_{axf}$  was above the threshold value. Estimates of the target centroid locations with respect to the actual centroid locations, the reconstructed target volume, and the difference between the actual and reconstructed target positions are provided in Table 3. The volume of the reconstructed target was sensitive to the threshold value of the reconstructed parameter, although there was a minimum effect of the threshold value on the reconstructed target's centroid location.

Although the volume of the actual target(s) comprised 0.6% or less of the total volume that was tomographically imaged, the target(s) was reconstructed

close to its true location(s) with minimal or no artifacts, as shown in Figures 3–6 and quantified in Table 3. However, in the imperfect-uptake experiments (ie, those in which the T:B ratio was 100:1), the reconstructed depth of the target was underestimated as the actual depth of the target increased.

The effect of discretization of the finite-element mesh in the reconstruction of the tissue phantom is shown in Figures 6 and 7 for the fourth experiment, which involved small-volume and multiple targets in conditions of perfect uptake (T:B ratio, 1:0). Figures 6 and 7 show anterior and lateral views of the reconstructed

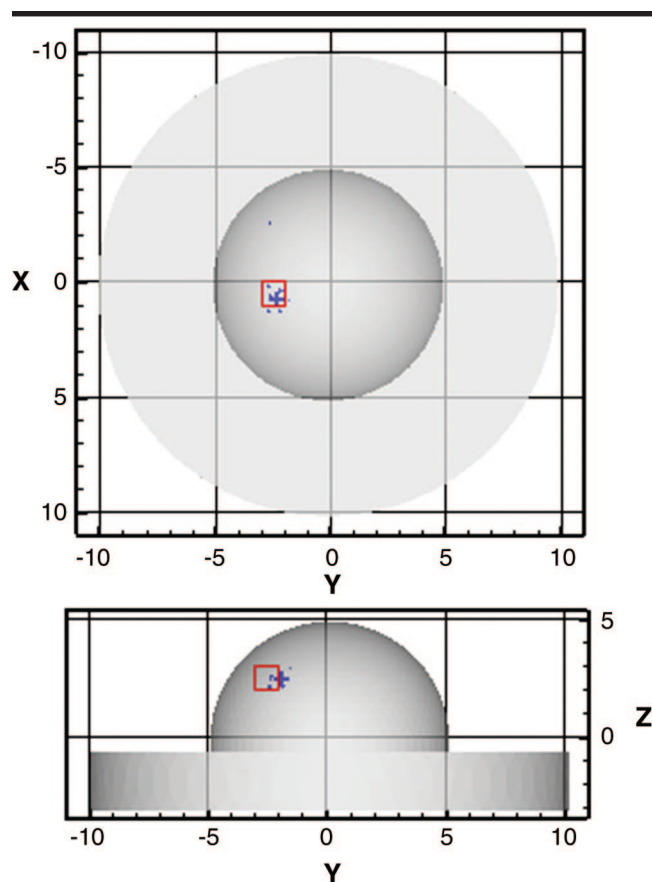


**Figure 3.** Anterior (top) and lateral (bottom) views of reconstructed tissue phantom for experiment 1. The actual 1.0-cm<sup>3</sup> target, located 1.43 cm deep with a T:B ratio of 100:1, is indicated by the solid red square, and the reconstructed target is indicated by blue points at the corresponding nodes in the finite-element mesh. Sizes of the blue symbols are directly proportional to the intensities of the reconstructed parameter  $\mu_{axf}$ .

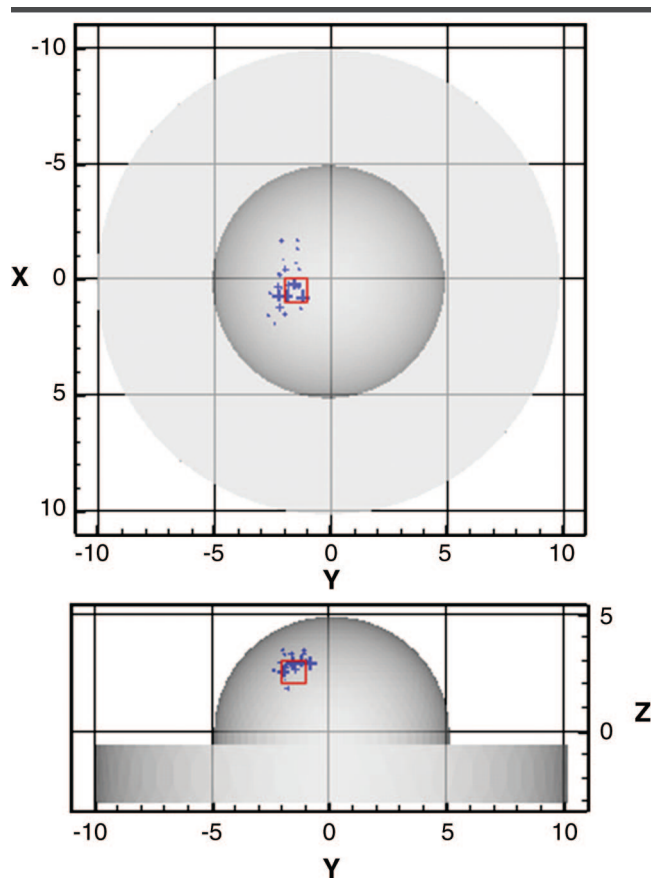


**Figure 4.** Anterior (top) and lateral (bottom) views of reconstructed tissue phantom for experiment 2. The actual 1.0-cm<sup>3</sup> target, located 2.04 cm deep with a T:B ratio of 100:1, is indicated by the solid red square, and the reconstructed target is indicated by blue points at the corresponding nodes in the finite-element mesh. Sizes of the blue symbols are directly proportional to the intensities of the reconstructed parameter  $\mu_{axf}$ .

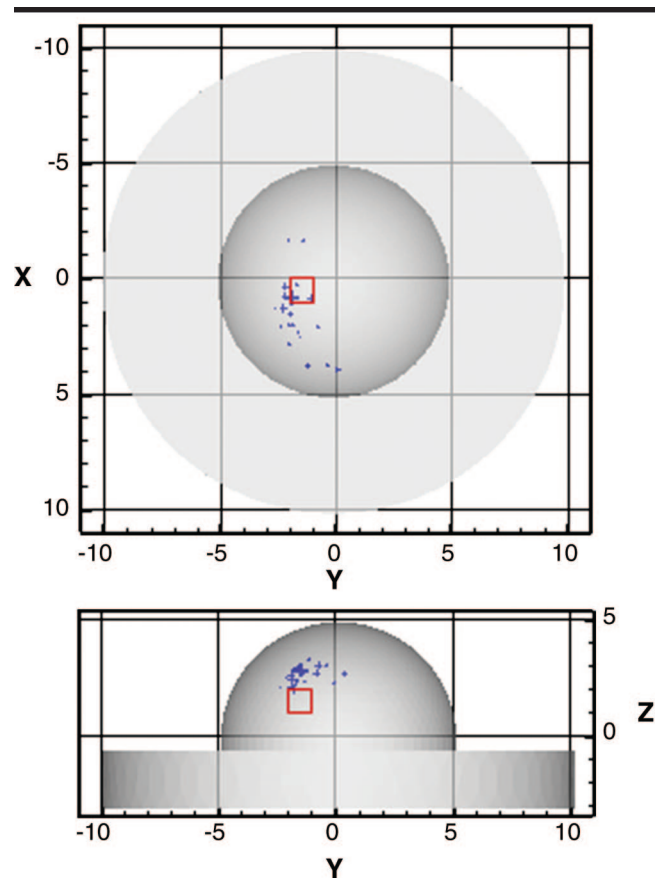


**Figure 5.** Anterior (top) and lateral (bottom) views of reconstructed tissue phantom for experiment 3. The actual 1-cm<sup>3</sup> target, located 2.82 cm deep with a T:B ratio of 100:1, is indicated by the solid red square, and the reconstructed target is indicated by blue points at the corresponding nodes in the finite-element mesh. Sizes of the blue symbols are directly proportional to the intensities of the reconstructed parameter  $\mu_{axf}$ .

breast phantom obtained by using a finite-element mesh with 11 906 and 3857 unknowns, respectively. These figures show the reconstructed targets, which are detected on the basis of the spatial distribution of nodal points that have values of  $\mu_{axf}$  that are above the threshold values. The estimated centroids and the difference between the actual and reconstructed target positions for the multiple-target experiment (experiment 4) are provided for the fine discretized mesh (11 906 unknowns) in Table 3. The reconstructions of the small-volume multiple targets that were performed by using the finite-element mesh with 3857 unknowns did not yield distinctly reconstructed targets.

## DISCUSSION

Unlike the situation with conventional nuclear imaging, magnetic resonance imaging, positron emission tomography,

and CT, the translation of NIR optical imaging with fluorescent contrast agents from the laboratory to the clinic requires the simultaneous introduction of both new investigational imaging agents and a new investigational imaging device. Questions regarding (a) the ability of this method to enable detection of the small fluorescent signals generated from deeply located targets at the tissue surface, (b) the influence of measurement noise on tomographic image reconstruction algorithms, and (c) the local quantities of the contrast agent required for enhancement need to be assessed in phantoms with clinically relevant sizes before clinical translation can be attempted.

The results of our study demonstrate the feasibility of optical tomographic imaging of single and multiple fluorescently contrasted lesions by using surface measurements of re-emitted fluorescent light generated by a micromolar concentration of ICG, an agent with Food and

Drug Administration approval for the indications of assessing hepatic function and retinopathy.

Currently, several limitations hinder the capabilities of fluorescence-enhanced optical tomography. First and foremost, the "noise floor" attributable to excitation light leakage through the rejection filters remains the critical factor for increasing the penetration depth and reducing the contrast or amount of contrast agent required for target detection. For example, the excitation light that reaches the end of a fiber optic is at least three or four orders of magnitude higher than the fluorescent signal collected in our experiments. Rejection of excitation light with interference filters with "typical" optical densities of 4 or 5 will result in a high noise floor and limit the sensitivity of detecting deep or weakly fluorescing lesions.

While the use of frequency-domain photon migration measurements alleviates the noise floor problem due to am-

**TABLE 3**  
Quantitative Estimates of Reconstructed Phantom Parameters for All Experiments

Experiment No. and True Target Depth (cm)	True Target Volume (cm <sup>3</sup> )	Reconstructed Volume (cm <sup>3</sup> )	True Centroid Locations in x, y, z Planes (cm)	Reconstructed Centroid Locations in x, y, z Planes (cm)	Difference in Centroid Location (cm)
1	1.43	1.0	0.5, -2.5, 2.5	0.4, -2.2, 2.6	0.32
2	2.04	1.0	0.5, -1.5, 2.5	0.2, -1.7, 3.0	0.64
3	2.82	1.0	0.5, -1.5, 1.5	1.3, -1.5, 2.8	1.50
4	1.37	About 0.55	-1.0, -3.0, 1.8	-1.0, 3.0, 2.2	0.46
	1.35	About 0.55	-1.0, 2.0, 2.9	-1.0, 2.1, 3.0	0.21
	1.27	About 0.55	2.0, -1.0, 3.0	2.0, -1.0, 3.0	0.06

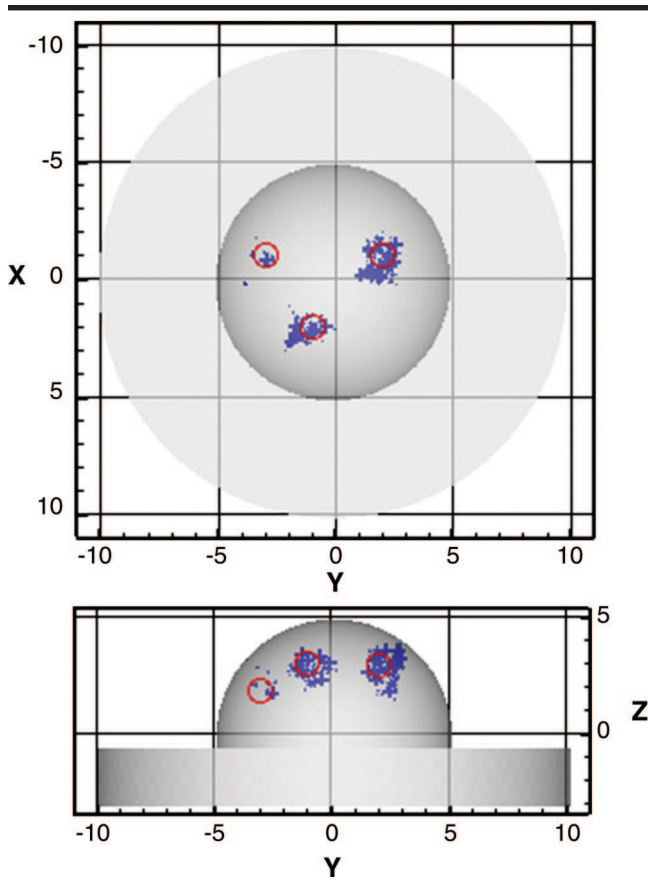


**Figure 6.** Anterior (top) and lateral (bottom) views of reconstructed tissue phantom for experiment 4. The actual three approximately 0.55-cm<sup>3</sup> targets, located about 1.30 cm deep with a T:B ratio of 1:0, are indicated by the solid red circles, and the reconstructed targets are indicated by blue points at the corresponding nodes in the finite-element mesh. Sizes of the blue symbols are directly proportional to the intensities of the reconstructed parameter  $\mu_{\text{axf}}$ . Here, a finely discretized finite-element mesh (11 906 unknowns) was used during reconstructions.

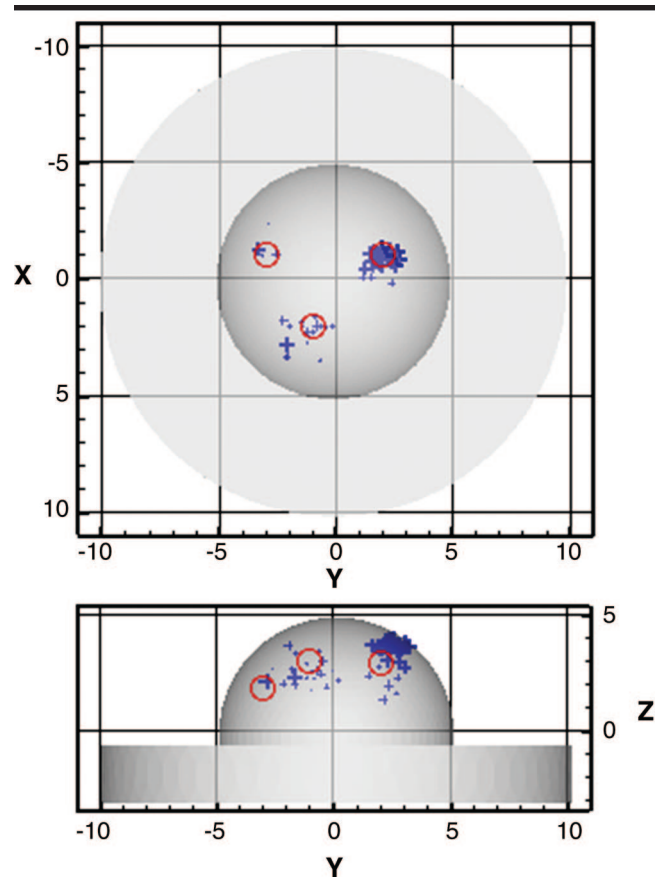


**Figure 7.** Anterior (top) and lateral (bottom) views of reconstructed tissue phantom for experiment 4. The actual three approximately 0.55-cm<sup>3</sup> targets, located about 1.30 cm deep with a T:B ratio of 1:0, are indicated by the solid red circles, and the reconstructed targets are indicated by blue points at the corresponding nodes in the finite-element mesh. Sizes of the blue symbols are directly proportional to the intensities of the reconstructed parameter  $\mu_{\text{axf}}$ . Here, a coarse discretized finite-element mesh (3857 unknowns) was used during reconstructions.

bient light in comparison to time-domain or continuous wave measurements (18), excitation light leakage remains a limitation of all optical techniques. This limitation restricts the reconstruction of deeply located targets containing smaller

amounts of fluorophore for contrast. Frequency-domain photon migration measurements have been shown to reveal the presence of a 100- $\mu\text{L}$  volume containing 100 fmol of ICG located as deep as 4 cm in a phantom-based study (18). However,

owing to excitation light leakage through the interference filters, the weak fluorescent signal is not quantitatively accurate for tomographic image reconstruction. Advances in filter design and implementation could overcome this limitation.

The final image resolution of fluorescence-enhanced imaging depends on the discretization of the finite-element mesh. One of the challenges for fluorescence-enhanced optical tomography is resolution: The greater the resolution, the greater the number of unknowns that will result, and, henceforth, the more computationally difficult the tomography problem will be. The development of tomographic imaging algorithms that are capable of handling high-spatial-resolution imaging, involving adaptive meshing and boundary element methods, may further improve computational efficiency and is currently being investigated.

The development of NIR-excitable probes conjugated to targeting ligands and reporting agents is paramount for fluorescence-enhanced molecular optical tomography. While there has been much progress in molecular imaging with nuclear techniques, fluorescent probes coupled with fluorescence-enhanced tomography may offer greater imaging sensitivity owing to the repeated activation, relaxation, and re-emission of fluorescent photons by NIR fluorophores. Consequently, the use of conjugated NIR fluorophores yields improved signal-to-noise ratios as compared with the signal-to-noise ratios yielded by signal-conjugated radiotracers, which are extinguished after a single emission event. The reader is referred elsewhere for reviews of the molecularly targeting and reporting fluorescent contrast agents being developed (19–21).

In conclusion, in this study, 3D optical tomographic reconstructions were performed on the basis of experimental data obtained in a phantom with clinically relevant geometry that contained targets contrasted by micromolar ICG at varying depths (1.43–2.82 cm deep) or multiple 0.55-cm<sup>3</sup> targets located approximately 1.30 cm deep. Further work to improve depth of penetration, resolution, and imaging contrast by using improved meth-

ods for achieving excitation light rejection, as well as adaptive finite-element or boundary element methods for improved computational analysis, is underway.

These preliminary data on fluorescence-enhanced optical imaging of large breast phantoms demonstrate its potential benefit for clinical applications. Future work involves algorithm improvement of image resolution, conjugation of ICG-like molecules for molecular targeting, and improved rejection of excitation light for accurate collection of fluorescent light signals.

#### References

- Weissleder R. Molecular imaging: exploring the next frontier. *Radiology* 1999; 212:609–614.
- Ntziachristos V, Weissleder R. Experimental three-dimensional fluorescence reconstruction of diffuse media by use of a normalized Born approximation. *Opt Lett* 2001; 26:893–895.
- Eppstein MJ, Hawrysz DJ, Godavarty A, Sevick-Muraca EM. Three-dimensional near-infrared fluorescence tomography with Bayesian methodologies for image reconstruction from sparse and noisy data sets. *Proc Natl Acad Sci U S A* 2002; 99:9619–9624.
- Hawrysz DJ, Eppstein MJ, Lee J, Sevick-Muraca EM. Error consideration in contrast-enhanced three-dimensional optical tomography. *Opt Lett* 2001; 26:704–706.
- Lee J, Sevick-Muraca EM. Three-dimensional fluorescence enhanced optical tomography using referenced frequency-domain photon migration measurements at emission and excitation wavelengths. *J Opt Soc Am A Opt Image Sci Vis* 2002; 19:759–771.
- Godavarty A, Eppstein MJ, Zhang C, et al. Fluorescence-enhanced optical imaging in large tissue volumes using a gain modulated ICCD camera. *Phys Med Biol* 2003; 48:1701–1720.
- Leevy CM, Smith F, Longueville J. Indocyanine green clearance as a test for hepatic function: evaluation by dichromatic ear densitometry. *JAMA* 1967; 200:236–240.
- Kogure K, David NJ, Yamanouchi U, Choromokos E. Infrared absorption angiography of the fundus circulation. *Arch Ophthalmol* 1970; 83:209–214.
- Sevick-Muraca EM, Lopez G, Reynolds JS, Troy TL, Hutchinson CL. Fluorescence and absorption contrast mechanisms for biomedical optical imaging using frequency-domain techniques. *Photochem Photobiol* 1997; 66:55–64.
- Thompson AB, Sevick-Muraca EM. Near-infrared fluorescence contrast-enhanced imaging with intensified charge-coupled device homodyne detection: measurement precision and accuracy. *J Biomed Opt* 2003; 8:111–120.
- Lakowicz JR, Berndt KW. Lifetime-selective fluorescence imaging using an rf phase-sensitive camera. *Rev Sci Instrum* 1991; 62:1727–1734.
- Reynolds JS, Troy TL, Sevick-Muraca EM. Multipixel techniques for frequency-domain photon migration imaging. *Bio-technol Prog* 1997; 13:669–680.
- Fedele F, Laible JP, Eppstein MJ. Coupled complex adjoint sensitivities for frequency-domain fluorescence tomography: theory and vectorized implementation. *J Comput Phys* 2003; 187:597–619.
- Sevick EM, Burch CL. Origin of phosphorescence signals reemitted from tissues. *Opt Lett* 1994; 19:1928–1930.
- Patterson MS, Pogue BW. Mathematical model for time-resolved and frequency-domain fluorescence spectroscopy in biological tissues. *Appl Opt* 1994; 33:1963–1974.
- Hutchinson CL, Lakowicz JR, Sevick-Muraca EM. Fluorescence lifetime based sensing in tissues: a computational study. *Biophys J* 1995; 68:1574–1582.
- Eppstein MJ, Dougherty DE, Hawrysz DJ, Sevick-Muraca EM. 3-D Bayesian optical image reconstruction with domain decomposition. *IEEE Trans Med Imaging* 2001; 20:147–163.
- Houston JP, Thompson AB, Gurfinkel M, Sevick-Muraca EM. Sensitivity and depth penetration of continuous wave versus frequency-domain photon migration near-infrared fluorescence contrast-enhanced imaging. *Photochem Photobiol* 2003; 77:420–430.
- Sevick-Muraca EM, Houston JP, Gurfinkel M. Fluorescence-enhanced, near infrared diagnostic imaging with contrast agents. *Curr Opin Chem Biol* 2002; 6:642–650.
- Licha K. Contrast agents for optical imaging. *Top Curr Chem* 2002; 222:1–29.
- Bremer C, Ntziachristos V, Weissleder R. Optical-based molecular imaging: contrast agents and potential medical applications. *Eur Radiol* 2003; 13:231–243.